

# Interpolation Volume Calibration: A Multisensor Calibration Technique for Electromagnetic Trackers

Henry Himberg, Yuichi Motai, *Member, IEEE*, and Arthur Bradley

**Abstract**—AC electromagnetic trackers are well suited for head tracking but are adversely affected by conductive and ferromagnetic materials. Tracking performance can be improved by mapping the tracking volume to produce coefficients that correct position and orientation (PnO) measurements caused by stationary distorting materials. The mapping process is expensive and time consuming, requiring complicated high-precision equipment to provide registration of the measurements to the source reference frame. In this study, we develop a new approach to mapping that provides registration of mapping measurements without precision equipment. Our method, i.e., the interpolation volume calibration system, uses two simple fixtures, each with multiple sensors in a rigid geometry, to determine sensor PnO in a distorted environment without mechanical measurements or other tracking technologies. We test our method in a distorted tracking environment, constructing a lookup table of the magnetic field that is used as the basis for distortion compensation. The new method compares favorably with the traditional approach providing a significant reduction in cost and effort.

**Index Terms**—AC magnetic tracking, magnetic tracker calibration, position and orientation measurements.

## NOMENCLATURE

Symbol	Definition
AR	Augmented Reality.
$f_D(r)$	Dipole Formula for the signal matrix at field point $r$ .
$f_I(r)$	A function that determines the secondary field of field point $r$ in the interpolation volume.
$f_S(r)$	The estimated signal matrix measured at field point $r$ inside the interpolation volume.
$f_{STS}(S)$	A function that computes the product of the signal matrix $S$ transpose and the signal matrix.
$r$	A field point position vector ( $3 \times 1$ ).

Manuscript received October 4, 2011; revised March 8, 2012; accepted April 25, 2012. Date of publication May 30, 2012; date of current version September 28, 2012. This paper was recommended for publication by Associate Editor M. Minor and Editor B. J. Nelson upon evaluation of the reviewers' comments. This work was supported in part by the National Science Foundation under Grant ECCS #1054333 and by the School of Engineering, Virginia Commonwealth University, Richmond, VA.

H. Himberg is with the Polhemus, Inc., Colchester, VT 05446 USA (e-mail: hhimberg@polhemus.com).

Y. Motai is with the Department of Electrical and Computer Engineering, Virginia Commonwealth University, Richmond, VA 23284 USA (e-mail: ymotai@vcu.edu).

A. Bradley is with the Langley Research Center, National Aeronautics and Space Administration, Hampton, VA 23681 USA (e-mail: arthur.t.bradley@nasa.gov).

Color versions of one or more of the figures in this paper are available online at <http://ieeexplore.ieee.org>.

Digital Object Identifier 10.1109/TRO.2012.2198929

$G$	A $3 \times 3$ matrix containing the secondary (distortion) field.
$G^n$	The secondary field signal matrix of sensor $n$ of the interpolation fixture.
$g(r)$	The secondary field signal matrix (a $3 \times 3$ matrix) at field point $r$ .
IVC	Interpolation Volume Calibration.
LUT	Look up Table.
$q_0^n$	The quaternion orientation of sensor $n$ at time step 0 in the source reference frame.
$q_k^n$	The orientation of sensor $n$ at time step $k$ in the source reference frame.
$qB^n$	The relative orientation of sensor $n$ in the mapping fixture reference frame. This value is a constant after initialization at time step 0.
$qB_0^n$	The quaternion orientation of sensor $n$ on the mapping fixture, in the mapping fixture reference frame at time step 0.
$q^I$	The quaternion orientation of the interpolation frame.
$qF^n$	An interpolation fixture sensor orientation in the source reference frame.
$qF_0^n$	The quaternion orientation of sensor $n$ at time step 0 in the interpolation fixture reference frame.
$QtoT(q)$	A function that converts quaternion orientation $q$ to a rotation matrix.
PnO	Position and Orientation.
$r_0^n$	The position vector of sensor $n$ at time step 0.
$rI, r2$	A sensor to sensor vector on the interpolation fixture used to define the fixture frame.
$r_k^n$	The position of sensor $n$ in the source reference frame at time step $k$ .
$rB^n$	The relative position of sensor $n$ in the mapping fixture reference frame. This value is a constant after initialization at time step 0.
$rF^n$	A fixture sensor position in the source reference frame.
$rP$	Sensor position on the interpolation fixture in the fixture frame of reference.
$S$	A $3 \times 3$ matrix of normalized field measurement.
$S_{meas}$	The measured signal matrix (a $3 \times 3$ matrix).
$StS$	The product of the signal matrix transpose ( $S^T$ ) and the signal matrix ( $S$ ).
$TtoQ(T)$	A function that converts a rotation matrix $T$ to a quaternion orientation.
$T$	Rotation matrix ( $3 \times 3$ ).
$T^I$	A rotation matrix representing the orientation of the interpolation fixture in the source reference frame.

$T^M$	The orientation of sensor $O$ on the mapping fixture, expressed as a rotation matrix (this is also defined as the mapping fixture reference frame).
$T^S$	A sensor orientation matrix.
VR	Virtual Reality.
$\Lambda$	The error in the estimated signal matrix.

TABLE I  
DISTORTION LEVELS

Distortion Level	Position Error (mm)	Orientation Error (milliradians)
Mild	Less than 5 mm	Less than 100
Moderate	5 to 20 mm	100 to 500
Severe	More than 20 mm	More than 500

## I. INTRODUCTION

VIRTUAL reality and augmented reality (VR/AR) systems are often used to immerse robot operators in the robotic environment [5], [14], [28], [32]. The VR/AR system combines information from different sensors and/or camera views into a single display system to improve situational awareness [9], [22], [24]. Sophisticated VR/AR environments use head tracking to provide situation-dependent enhancements, such as virtual objects and symbology [1]. AC magnetic trackers provide an ideal platform for head tracking in these environments [17] but can have large errors if conductive or ferrous materials are nearby. Tracking errors can be corrected using a map of the tracking volume that characterizes the position and orientation (PnO) errors, but the mapping process is expensive and/or time consuming. The need to maintain accurate registration between the measured PnO and true PnO requires complex equipment that is often difficult to use resulting in an expensive, time-consuming operation.

AC magnetic trackers are adversely affected when nearby objects distort the tracker generated magnetic field. A study of the effect of conductive and ferromagnetic materials on magnetic trackers was conducted by Nixon *et al.* [29]. Distortion effects were seen to be highly dependent on the geometry of the source and sensor. Careful control of the source and sensor locations can be used to minimize stationary distortion [2], [18], [19], [26], [33]; nonstationary distorters must be removed from the tracking volume through the use of alternative materials (stainless steel or acrylic).

The effect of stationary distorting material on tracker measurements can be classified by the maximum orientation error found in the tracking volume (see Table I). Mild distortion levels occur in applications where distorting materials near the tracking volume exert a weak influence that causes small position errors (<5 mm) but up to 100 mrad of orientation error. A VR/AR environment that has been carefully built without distorting materials but has small metal objects just outside of the tracking volume often has mild distortion. Moderate distortion levels occur when large conductive or ferrous materials are located at the edges of the tracking volume, causing position error of up to 20 mm and orientation errors less than 500 mrad. This situation occurs when the VR/AR environment has large metal structures located just outside of the tracking volume that are not near the magnetic source. Severe distortion occurs when the tracking volume is surrounded by or includes large metal structures that are mechanically linked together and are positioned near the magnetic source. A VR/AR application that is installed in a confined space surrounded by metal structure (such as a vehicle or aircraft) often results in severe distortion with position errors of 50 mm or more and orientation errors of more than 1 rad.

The errors that are caused by distortion can be corrected using various methods including polynomial functions and lookup tables (LUTs). A description of several distortion compensation schemes is presented by Kindratendo [23] and Raab *et al.* [30]. All of these techniques require data collection using the tracker to create a map of errors as a function of true PnO. The mapping process requires locating the sensor at a multitude of positions in the volume, while maintaining registration of the measured PnO to the true PnO. Registration is accomplished through either use of a hybrid tracker that combines an undistorted measurement with the electromagnetic tracker measurement or through mechanical means that precisely determine the sensor PnO.

A hybrid tracker combines the ac electromagnetic tracker with a nonmagnetic tracking technology to accurately measure PnO during the mapping process. This approach eliminates the need for precise location of the sensor during the mapping, simplifying the equipment at the expense of a second tracking technology. Optical tracking is often used in hybrid approaches where its high accuracy is beneficial and occlusions are not a factor due to the offline nature of the mapping process. A hybrid tracking system consisting of a magnetic sensor for tracking and an optical sensor for registration was proposed by Nakada *et al.* [27]. The system was used to map a tracking environment and select one of four polynomial correction functions based on the distortion level. This approach reduced errors from 40 mm to less than 2 mm. A similar system proposed by Birkfellner *et al.* [3] using an emitter/detector optical tracking system showed improvement in accuracy of the magnetic tracker to an average error of 2.8 mm as compared with 4.6 mm for the uncompensated case. Another approach using multiple magnetic sensors with an optical marker/camera system for registration was presented by Feuerstein *et al.* [8]. Their approach reduced composite root means square (RMS) position error from 6.91 to 3.15 mm without calibration. Ikits *et al.* [20] also combined an electromagnetic tracker with infrared marker/camera registration in their study on distortion compensation. The system reduced average position error from 42.3 to 4.82 mm and average orientation error from 185 to 16.2 mrad. Although optical trackers are commonly used to create hybrid tracking systems, other technologies can be used for registration. A mapping system using an ultrasonic sensor for registration was proposed by Ghazisaedy *et al.* [13]. The method reduced position errors to less than 5% of the measured distance but did not significantly improve on small errors due to a lack of precision in the registration system. A mapping process combining optical and mechanical registration with magnetic tracking was used by Fisher [10]. This system used optical tracking to calibrate a

mechanical fixture used in the mapping procedure. Hybrid systems, particularly those using optical tracking, can provide sufficiently precise registration for mapping but at increased cost and complexity.

Mechanical registration avoids the complexity of hybrid registration through use of nondistorting fixtures with known geometry. Kindratenko and Sherman [31] used a system of interlocking polyvinyl chloride pipes in various lengths to create a low-cost registration method in their mapping experiments. Their method provided 1 cm of accuracy but was time consuming due to the constant assembly and disassembly of the pipes. A calibration technique using a pegboard and jig to provide mechanical registration was used by Day *et al.* [7]. The system reduced errors to an average of 1.8 cm and  $1.2^\circ$  at a range of up to 1.8 m from the magnetic source. Another pegboard scheme with holes at 12-in intervals was proposed by Bryson [4]. The collected data were used to evaluate three compensation schemes and found to reduce a 4-in average error to 2 in. Livingston and State [25] used a Faro mechanical tracking system (Faro arm) to provide mechanical registration during data collection. The system reduced average position error by 79% and average orientation error by 40%. Mapping with mechanical registration is time consuming but can be improved through the adoption of automated (robotic) devices. Automated mapping devices can reduce data collection time but are expensive to construct and complex to operate. Another approach to this problem is to use multiple sensors to simultaneously collect data.

Multiple sensors reduce data collection time and, if in a known geometry, add constraints that can detect distortion. Hagemester *et al.* [16] used multiple sensors in a known geometry to measure errors for real-time PnO corrections. Their technique generated correction factors by comparing the known distance between sensors with the measurements to correct PnO by more than 50% without a formal mapping. A method of calibrating a volume using multiple sensors attached to a rigid object was proposed by Wu and Taylor [35]. Their system reduced position errors from 2.05 to 0.80 mm and orientation error from 13 to 7.9 mrad. Another multiple sensor system using six magnetoresistive sensors was proposed by Wang and Jiang [34]. The sensors were mounted on opposing sides of a cube and paired to produce two position measurements with a known relative distance. When used in the tracking environment, the position of the center of the cube was calculated as the weighted sum of the sensor pairs.

The additional constraints available through multiple sensor techniques present an opportunity to improve mapping techniques. We combine these constraints with a new registration technique to dramatically reduce the cost and complexity of the mapping process. Our method, i.e., the interpolation volume calibration (IVC) uses multiple sensors in a fixed geometry to simultaneously collect data through registration of a single sensor. A new registration method using real-time distortion compensation eliminates the need for mechanical or hybrid registration approaches.

Our contribution is several fold:

- 1) a novel method of correcting distorted PnO measurements in real time without mapping;
- 2) a new metric for determining the error in ac magnetic tracker position estimates from field data;
- 3) a data collection process that can be used to create an LUT without costly mapping equipment.

We provide background on the PnO algorithms used in ac magnetic trackers in Section II. The mathematical basis for our system is developed in Section III along with data collection process and offline processing algorithm used to construct the LUT. Our method is tested in Section IV, and experimental results are discussed. In Section V, we draw conclusions on how our method relates to the calibration problems.

## II. BACKGROUND

An ac electromagnetic tracker determines PnO by generating a 3-D ac magnetic field and measuring the mutual inductance between sensor/source pairs. The magnetic field source and sensor are constructed of three concentric, orthogonal coils. The tracker measures the voltage induced on each of the sensor coils and normalizes the data to the source/sensor assemblies, operating frequency, and various physical constants. The data are represented by a  $3 \times 3$  signal matrix  $S$  containing the normalized field measurements for each of the nine source/sensor coil pairs. An algorithm presented by Jones [21] provides a simplified relationship between the signal matrix and PnO (1). The measured signal matrix  $S$  is the product of the transposed sensor rotation matrix in the source frame  $T$  and the unrotated dipole field  $f_D(r)$ . Note that several physical constants, the magnetic field frequency, and other parameters have been removed from the equation through calibration of the source and sensor

$$S = (T)^T f_D(r). \quad (1)$$

The dipole field, shown in (2) below, calculates the signal matrix based on the outer product  $\langle rr^T \rangle$  of the position vector  $r$ . We refer to (2) as the *unrotated* signal matrix, since it assumes that the sensor is aligned to the source frame, with the position vector describing the offset between the sensor magnetic moment and the source magnetic moment

$$f_D(r) = (1/\|r\|^3) (3\langle rr^T \rangle / \|r\|^2 - I). \quad (2)$$

The continuous magnetic fields used in ac magnetic trackers induce eddy currents in nearby conductive materials which generate secondary magnetic fields that distort the primary (dipole) field created by tracker [15]. Ferrous materials cause distortion by warping the magnetic flux lines, reducing the applicability of the dipole field model. Without the secondary magnetic field, the sensor winding voltage is a function of the position of the sensor in the source frame. With the secondary field present, the dipole equation no longer applies, since the voltage at the sensor is a function of both the primary and secondary magnetic fields. The measured signal matrix  $S$  is now the sum of the primary field  $f_D(r)$  and secondary field  $G$  rotated by the transpose of the sensor rotation  $(T)^T$  in the source frame

$$S = (T)^T (f_D(r) + G). \quad (3)$$

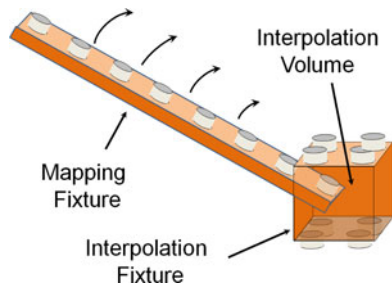


Fig. 1. Mapping fixture is used to simultaneously collect field data at multiple positions and orientations while using the interpolation volume to provide registration to the source reference frame.

The superposition of the primary and secondary fields in the tracking environment provides the opportunity to compensate the tracker measurement by subtracting the secondary field from the measurement before the PnO computation. This model assumes that the sensor is not attached to a ferrous or conductive material which would make the secondary field pickup orientation dependent.

### III. FIELD MAPPING USING INTERPOLATION VOLUME CALIBRATION

The IVC system creates a secondary field LUT that can be used for field compensation or to develop data for other compensation methods. The system uses two fixtures, i.e., the interpolation fixture and the mapping fixture, to collect a “data cloud” of field points that are then interpolated to construct a uniform grid LUT of the secondary magnetic field (see Fig. 1). The data collection is performed using sweeping motions of the mapping fixture, while using the interpolation fixture to provide registration of the collected data to the source reference frame. The system is built on the premise that an LUT can be aligned to an arbitrary reference frame by including any alignment errors in the compensation coefficients, removing the requirement for absolute measurement accuracy in the mapping process. The user determines the LUT alignment and the measurement reference frame when the interpolation fixture is placed in the mapped volume. The interpolation fixture also defines a small volume in which the PnO of a sensor at an arbitrary field point can be determined.

Once the interpolation volume is defined, the mapping fixture collects field data throughout the mapped volume. The PnO of the mapping fixture sensors are extrapolated from the interpolation volume through the known fixed geometry of the fixture. Development of the interpolation volume concept and fixture design is discussed in Section III-A. The mapping fixture and an analysis of measurement errors are developed in Section III-B. Section III-C develops the field data-collection process, providing detail on how the two fixtures are used to collect field data. In Section III-D, the algorithm to generate the LUT is developed.

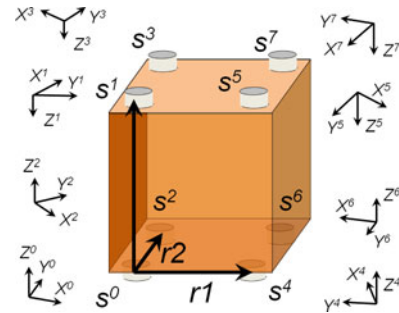


Fig. 2. Interpolation fixture shown with eight sensors placed to construct a cube with a sensor at each vertex. The averaged positions of sensors 0, 1, and 4 are used to construct a fixture reference frame. The measured field at each fixture sensor is at a different orientation in the source reference frame and must be rotated into alignment with the source.

#### A. Interpolation Volume

The interpolation volume is a cube or a rectangular cuboid with a known PnO in the magnetic source reference frame and an edge dimension of approximately 40 mm. The small-edge dimension allows for the accurate estimation of the secondary field inside the volume using interpolation. The measured field for any point inside the volume can be estimated as the sum of the interpolated secondary field and the dipole field (3). Combining the field estimation with a cost function minimization process provides a mechanism to find the PnO of an arbitrary point inside the volume.

To create the interpolation volume, a small fixture is constructed to position a sensor on each vertex of a cube or near cube (rectangular cuboid) (see Fig. 1). The interpolation fixture is calibrated by measuring the PnO of each sensor with the tracker in a nondistorting environment. A nondistorting environment can be found by placing the fixture (and the magnetic source) at least 1.2 m away from any conductive/ferrous materials. During calibration, the fixture is placed at an arbitrary position in the source reference frame, while a large set (>100) of sensor PnO measurements are captured and then used to determine the relative sensor PnO on the fixture.

The PnO of sensor  $n$  on the interpolation fixture is found from the measured sensor positions by constructing a reference frame  $T^I$  using vectors  $r1$  and  $r2$  (see Fig. 2). The relative position of sensor  $n$  on the fixture  $rP^n$  is offset from sensor 0, rotated into the fixture reference frame (4), shown below. The relative orientation of sensor  $n$  on the fixture is found by rotating the measured orientation  $q_0^n$  into the fixture reference frame using quaternion multiplication (5) [6] shown below. We use the function  $TtoQ()$  to convert a rotation matrix to a quaternion value (6), shown below:

$$rP^n = T^I (r_0^n - r_0^0) \quad (4)$$

$$qP_o^n = (q^I)^{-1} q_0^n \quad (5)$$

$$q^I = TtoQ(T^I). \quad (6)$$

After calibration, the interpolation fixture is placed in the tracking environment, the fixture reference frame is aligned with the source reference frame, and the PnO of the fixture

in the magnetic source reference frame is declared by the user. The declared PnO should be within 10 mm for the true position and 100 mrad of the true orientation (both composite values). Inaccuracies in the declared PnO appear as additional distortion of the magnetic field and will be compensated for in the estimation process as an additional secondary field component. Theoretically, the system should be able to handle any inaccuracies, but these errors increase the nonlinearity of the system and can impact the accuracy of secondary field estimates.

The position of fixture sensor  $n$  in the source frame  $rF^n$  is the sum of the sensor 0 position  $rF^0$  and the relative sensor position  $rP^n$ , rotated by the fixture rotation matrix  $T^I$  (7). The fixture sensor orientation is the product of the fixture orientation  $q^I$  and the relative orientation  $qP^n$  (8), shown below:

$$rF^n = (rF^0 + T^I rP^n) \quad (7)$$

$$qF^n = q^I qP^n. \quad (8)$$

Once the interpolation fixture is aligned to the source frame,  $J$  frames of field data ( $J > 100$ ) are collected to estimate the expected value of the measured signal matrix for each fixture sensor  $S^n$ . The measured signal matrix  $S^n$  is rotated into alignment with the source reference frame, and the unrotated dipole field (2) is calculated using sensor position  $rF_n$  (7). Rearranging (3), we can compute the secondary field as the difference between the measured signal matrix and the dipole field for the known position, i.e.,  $f_D(rF^n)$ . The known sensor orientation  $qF^n$  is used to rotate the measured signal matrix  $S^n$  into alignment with the source reference frame before subtracting the dipole field. The function  $QtoT()$  is used to perform a quaternion to rotation matrix conversion

$$G^n = QtoT(qF^n) S^n - f_D(rF^n). \quad (9)$$

The secondary field at any field point inside the cube  $g(r)$  can be estimated from the known values at the cube vertices  $G$  using an interpolation function (10) shown below. A complete expression for the measured field at any point inside the cube can be constructed as the sum of the dipole field  $f_D(r)$  and the interpolated secondary field  $g(r)$ , rotated by the sensor orientation ( $T^S$ : a rotation matrix) (11) shown below:

$$g(r) = f_I(r, rF, G) \quad (10)$$

$$f_S(r, q) = (T^S)^T (f_D(r) + g(r)). \quad (11)$$

The ability to calculate the measured signal matrix provides a method to estimate the PnO of any sensor in the interpolation volume. To find the position, we use the dot product of the signal matrix to construct an orientation invariant cost function. The cost function (13), shown below, minimizes the difference in the StS product (12), shown below, between the measured  $S_{meas}$  and estimated signal matrix:

$$f_{StS}(S) = S^T S \quad (12)$$

$$\arg \min [f_{StS}(S_{meas}) - f_{StS}(f_S(r, qI))]. \quad (13)$$

The sensor orientation is found using a second cost function that minimizes the difference between the measured signal matrix  $S_{meas}$  and a rotation of the estimated signal matrix at the

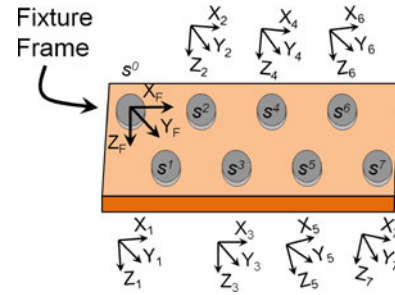


Fig. 3. Mapping fixture has multiple sensors located at regular intervals down the length of the material.

solved position  $r$  (14), shown below. Using (11), the position is kept constant at the value found using (13), while the quaternion orientation is varied

$$\arg \min [(f_S(r, q) - S)]. \quad (14)$$

The interpolation volume provides real-time correction of sensor PnO inside the interpolation volume without mapping the tracking volume. We use this method to provide registration of the mapping fixture without mechanical or hybrid methods.

### B. Mapping Fixture

The mapping fixture is constructed with sensors mounted at regular intervals down its length at arbitrary orientation (see Fig. 3). It is assumed that all eight sensors used for the interpolation fixture will be transferred to the mapping fixture. Additional sensors can be used to shorten the data collection process or improve sample density. The relative PnO of fixture sensors are measured through a calibration procedure similar to that used for the interpolation fixture. The mapping fixture reference frame is defined to be aligned with sensor 0, i.e., the reference sensor. Converting the sensor 0 orientation into a rotation matrix  $T^M$  (15), shown below, the position of sensor  $n$  relative to sensor 0 ( $rB^n$ ) is computed as the difference between the two positions, rotated into alignment with the fixture reference frame using  $T^M$  (16), shown below. The orientation of sensor  $n$  in the fixture frame, i.e.,  $qB^n$  is the quaternion product of the sensor  $n$  orientation  $q^n$  and the inverse of the sensor 0 orientation  $(q_0^0)^{-1}$ , both in the source reference frame (17), shown below:

$$T^M = QtoT(q_0^0) \quad (15)$$

$$rB^n = (T^M)^T (r_0^n - r_0^0) \quad (16)$$

$$qB_0^n = (q_0^0)^{-1} q_0^n. \quad (17)$$

Sensor PnO during the data collection process is determined through application of the estimated sensor 0 PnO to the relative PnO developed in (16) and (17). The position of sensor  $n$  at time step  $k$  is the relative position of sensor  $n$  ( $rP^n$ ) rotated by the sensor 0 orientation, i.e.,  $QtoT(q_k^0)$ , summed with the sensor 0 position  $r_k^0$  (18). The orientation of sensor  $n$  at time step  $k$  is the relative orientation of the sensor  $qB^n$ , rotated by the orientation

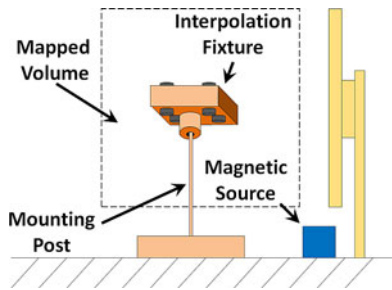


Fig. 4. Interpolation fixture is placed on a mounting post and aligned with the source reference frame before data collection.

of sensor 0  $q_k^0$  (19), shown below:

$$r_k^n = r_k^0 + QtoT(q_k^0) r B^n \quad (18)$$

$$q_k^n = q_k^0 q B^n. \quad (19)$$

Errors in the estimation of the sensor 0 PnO propagate through (17) and (18) and have an increasing effect on the estimated PnO of the mapping fixture sensor as the offset from sensor 0 increases. Position errors are indicated when there is a difference between the unrotated version of the estimated and measured signal matrices, leading to a nonzero result of the minimization equation. These errors are magnified on the mapping fixture when we determine the PnO of each sensor based on the reference sensor [12]. Although these differences are clearly related to the position error, they are obscured by the multiplications in (12). A better measure of the error in the position estimate is the difference between the estimated and measured signal matrices without rotation. The signal matrix estimate error  $\Lambda$  is calculated as the difference between the measured signal matrix  $S_{meas}$  and the estimated signal matrix (20), shown below. The measured signal matrix is rotated into alignment with the source reference frame using the estimated orientation  $q_{est}$ . The estimated signal matrix is the sum of the dipole field  $f_D(r)$  and the secondary field  $g(r)$  at the estimated position  $r_{est}$ :

$$\Lambda = (f_D(r_{est}) + g(r_{est})) - f_T(q_{est}) S_{meas}. \quad (20)$$

### C. Field Data Collection

The data collection process is performed in two phases: initialization of the interpolation volume and then the data collection itself. In the first phase, the interpolation fixture is used to define the interpolation volume in terms of PnO and secondary field values. The interpolation fixture is placed in a nondistorting environment and captures calibration data to determine the relative PnO of each sensor on the fixture. The interpolation fixture is then moved to the center of the mapped volume and aligned to the source reference frame (see Fig. 4). A large dataset of magnetic field measurements are made with the fixture to determine the secondary field value used in the interpolation process. Finally, the user declares the PnO of the fixture to establish a registration with the magnetic source reference frame.

In the second phase, the mapping fixture is used to collect a “cloud” of field points for the map generation process. Before data collection can begin, the mapping fixture is calibrated using

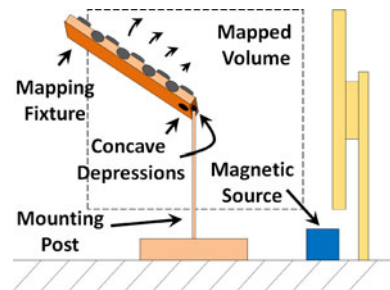


Fig. 5. Mapping fixture is designed to use the same mount as the interpolation fixture. The fixture has concave depressions that allow it to be rotated while keeping sensor 0 inside the interpolation volume.

the procedure outlined in Section III-B. Again, the calibration data are taken, while the fixture is stationary in a nondistorting environment. To collect data, the mapping fixture is positioned with sensor 0 that is inside the interpolation volume, while the fixture is slowly moved through the mapped volume (see Fig. 5). The data-collection process continues until a dense data cloud of points covering the entire mapped volume has been collected.

### D. Lookup Table Generation

The collected data consist of trajectories through the tracking volume that create a large set of scattered points, each with an associated magnetic field measurement. The PnO of sensor 0 is first found using the position cost function (13) and the orientation cost function (14). Once the sensor 0 PnO is known, the PnO of all the other sensors on the mapping fixture are found through the fixed geometry. The estimated sensor positions determine the secondary field at each point and create a data “cloud.” Natural neighbor interpolation is used to create a uniform grid LUT containing the secondary field for each grid point but alternative techniques [11] may be used.

## IV. EXPERIMENTAL RESULTS

A series of experiments was conducted to evaluate the expected performance of the IVC system. Each of the experiments use secondary field data collected from a typical application to approximate real-world results. The interpolation algorithm, mapping fixture, and data collection process are investigated in detail to determine expected errors. Overall system performance is evaluated by comparing compensated results based on IVC with uncompensated and polynomial corrected approaches.

### A. Experimental Data

IVC performance was evaluated using a 533 mm × 410 mm × 305 mm tracking volume located directly in front of a large LCD screen (see Fig. 6). The mapped volume is considered a severely distorted environment based on dipole algorithm orientation errors as large as 3800 mrad (see Table I). A Polhemus magnetic field mapper was used to generate a uniform grid LUT containing the true position and secondary field of each grid point. The mapper is a robotic device that provides precise mechanical registration, while providing three-axis translation ability (static position errors with the mapper are less than those

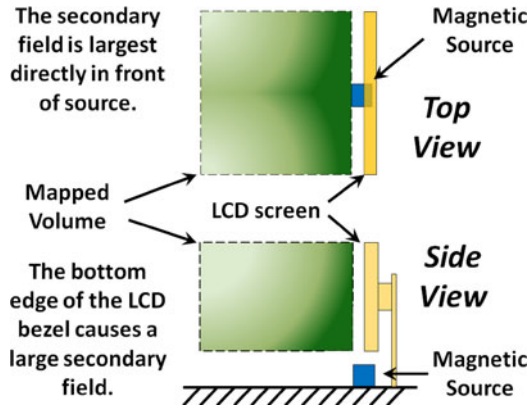


Fig. 6. Secondary field shown as a percentage of measured signal for our experimental data. The darker regions indicate a stronger field.

TABLE II  
PnO MEASUREMENT EQUIPMENT ACCURACY SPECIFICATION

Equipment	Static position Error (mm)	Static Orientation Error (milliradians)
mapper	< 0.25	< 1.4
tracker	0.71 (RMS)	2.6 (RMS)

TABLE III  
DATASET DISTORTION LEVELS

Category	Position Error (mm)	Orientation Error (milliradians)
mild	4.96 (11.20)	18.68 (47.31)
moderate	23.09 (51.18)	85.15 (110.79)
Moderate-severe	58.68 (125.76)	203.24 (524.94)
severe	105.45 (195.31)	642.70 (3753.00)

Note: Table entries are in RMS (MAX) format.

of the tracker; see Table II). The LUT was used to generate the measured field as the sum of the interpolated secondary field and the dipole field (3). The collected secondary field data were also used to create datasets for four different distortion levels by scaling the data until the desired dipole results were obtained (see Table III). The severe dataset was the unmodified data obtained when the LCD volume was mapped.

### B. Position and Orientation Estimation Using Interpolation

The accuracy of the PnO solution is dependent on the ability of the cost function minimization process to estimate the PnO in the interpolation volume. A trial data collection was conducted using a virtual interpolation cube placed in the center of the volume. The mapping fixture collected 100 000 samples of sensor PnO data, and the measured field of each point was estimated as the sum of dipole field and an interpolated secondary field, rotated by the measured sensor orientation (4). The PnO of each point was estimated using the cost function algorithms discussed in Section III-C. The interpolation function had a median position error of 0.27 mm and median orientation error of 1.50 mrad (see Table IV).

A histogram of the position errors [see Fig. 7(a)] shows that the majority of the points are grouped around 0.25 mm, but

TABLE IV  
PnO ERROR PROFILE

Measurement	Position (mm)	Orientation (milliradians)
median	0.27	1.50
75 percentile	0.50	2.40
Max	4.9	23.4

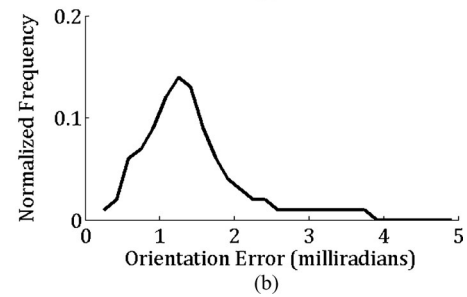
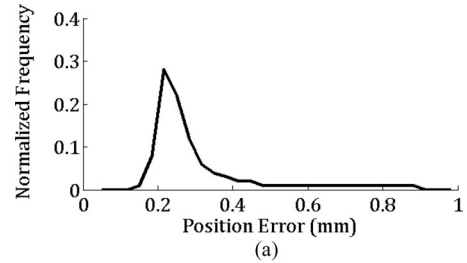


Fig. 7. Histograms of the (a) position error and (b) orientation error in interpolation estimates have a long tail of outlier values.

there is a long “tail” of large error values. Although most of the interpolation position errors were within the tracker error band (0.71 mm in Table II), there is a large group of outliers (position errors > 0.91 mm) with errors ranging as high as 4.9 mm. The orientation error has a less focused distribution [see Fig. 7(b)], and the majority of the points are larger than the maximum orientation error specified for the tracker (0.41 mrad; see Table II). The increased error in the orientation estimate is indicative of its dependence on the accuracy of the sensor position estimate. The orientation cost function (14) minimizes the error between the signal matrix at the estimated position and the measured signal matrix. When the position error is small, it has little effect on the orientation estimate, but when the error is large, the orientation estimate error increases dramatically. This relationship results in error accumulation in the orientation estimate, with a broader distribution and more outliers than the position error. The errors are related to at least two sources: the field data measurement itself and the inability of the cost function solver to converge on the correct answer at some field points. The larger errors are grouped in long smooth trajectories of sequential points with errors of 1 mm or more. These paths represent groups of solutions that diverge slightly due to convergence in local minima.

### C. Mapping Fixture Accuracy

The error at each sensor on the mapping fixture was estimated from the sensor 0 signal matrix error  $\Lambda$  (20) using the known

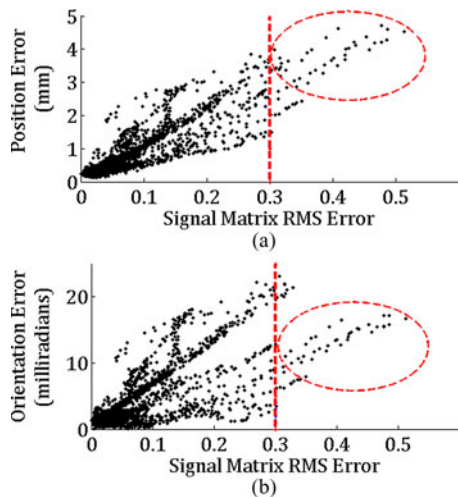


Fig. 8. PnO error of the interpolation estimate has a correlation to the RMS error of the unrotated signal matrix estimate. In this figure, we plot the (a) position and (b) orientation errors against the RMS average of the error in the unrotated signal matrix. The data appear in long strings of closely placed errors due to the combination of a high measurement rate (240 Hz) and slow motion of the fixture. Note the cluster of large error at the upper right corner of both plots, these groups of outliers are removed by imposing a maximum RMS error constraint of 0.3 on the estimated signal matrix.

TABLE V  
INTERPOLATION FIXTURE AVERAGE SENSOR POSITION ERRORS (in millimeters)

Sensor	0	1	2	3	4	5	6	7
X	0.0	-0.9	1.3	1.6	-1.2	0.0	0.9	1.7
Y	0.0	-2.2	-0.8	-1.4	0.0	-2.3	-2.9	-2.1
Z	0.0	-0.3	0.0	-3.3	0.0	-3.3	0.4	-3.3

geometry of the mapping fixture. As shown in Fig 8(a), the RMS of  $\Lambda$  has a strong correlation to the position error and can provide the basis for a correction of the position estimate. The orientation estimate also has a strong correlation to the signal matrix estimate that is well defined [see Fig. 8(b)] but is “looser” than that of the position error. A close examination of Fig. 8 reveals that the points with large errors are grouped together and can be separated from the majority of the data. Taking advantage of this separation, we imposed a maximum value of 0.300 on  $\Lambda$  for all data points.

#### D. Field Data Collection

An interpolation fixture was constructed from wood stock with precisely placed mounting holes for each sensor to align them with the vertices of the interpolation volume. The sensors do not have a precision mounting surface resulting in average position error of 1.26 mm (see Table V).

The interpolation cube size and rotation were optimized to best fit the measured data using an optimization function that varied the cube side dimension  $d$ , cube offset  $r$ , and orientation

TABLE VI  
OPTIMIZED INTERPOLATION FIXTURE SENSOR POSITION ERRORS (in millimeters)

Sensor	0	1	2	3	4	5	6	7
X	0.4	-0.9	0.3	0.2	-0.5	-0.2	0.2	0.6
Y	0.3	-1.7	0.2	-0.2	1.6	-0.4	-0.6	-0.5
Z	-0.2	2.1	-0.4	-1.1	0.2	-0.4	0.5	-0.6

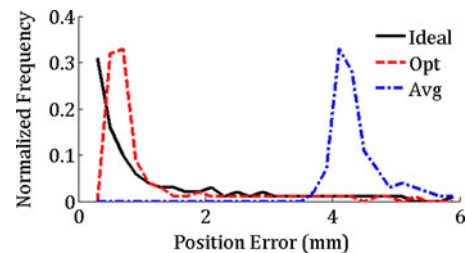


Fig. 9. Lack of a precision mounting surface on the sensor results in positioning errors on the interpolation fixture. Here, we see the position error distribution of mapping fixture sensor 8 (the furthest away from the interpolation volume) when using each of the three interpolation volumes (ideal, optimized, and averaged) to estimate sensor positions. Note the large reduction in error when using the optimized cube.

(in the fixture reference frame)  $T_C$ :

$$\arg \min [rP - T_C \Psi(r, d)] \quad (21)$$

$$\Psi(r, d) = r + d \begin{bmatrix} 0 & 0 & 0 & 0 & 1 & 1 & 1 & 1 \\ 0 & 0 & 1 & 1 & 0 & 0 & 1 & 1 \\ 0 & 1 & 0 & 1 & 0 & 1 & 0 & 1 \end{bmatrix}.$$

The interpolation cube optimization process removed most of the sensor placement errors, leaving a few offsets in the 1–2-mm range (see Table VI). The remaining errors do not have a large effect on accuracy because of their small magnitude as compared with the interpolation volume dimensions.

To gauge the importance of the sensor positions on the interpolation cube, a statistical analysis of position errors at random points in the interpolation volume was conducted. The test was run for 10 000 points of data captured in a nondistorting environment, while simulating data collection. Three interpolation cubes were considered: an “ideal” cube with no position errors, the “optimized” cube previously discussed, and a cube constructed from the “averaged” data without optimization. Looking at errors at the farthest sensor from the interpolation volume (see Fig. 9), it is seen that the ideal and optimized volumes reduce the median error but do not have the same impact on the larger errors (see Table VII).

The ideal volume does reduce the 95% confidence interval error by approximately 25%, but the optimization has almost no effect, suggesting that these errors are not related to the sensor positions on the fixture. These larger errors most likely correspond to specific areas in the interpolation volume, where

TABLE VII  
SENSOR 8 POSITION ERRORS VERSUS INTERPOLATION CUBE

Measurement	Ideal	Optimized	Averaged
Median	0.48	0.68	4.31
95 percentile	9.54	12.0	12.69
Max	16.8	16.4	16.7

the trilinear interpolation process has difficulty in estimating the secondary field data. The “trouble spots” may be localities that have a high degree of nonlinearity in the field data and are not well estimated.

The interpolation estimates are critical to the accuracy of the field measurements made with the mapping fixture and must be handled correctly to avoid large errors entering the LUT we are creating. Errors in the orientation estimates have a larger effect on the accuracy of the LUT, since they are multiplied by the displacement of sensors on the mapping fixture from sensor 0.

#### E. Lookup Table Generation

The IVC system LUT generation process was evaluated by mapping the LCD environment and then testing the accuracy of compensation based on the LUT at random points using field compensation (13). The data collection process took approximately 1 or 2 h, including time to gather calibration data for the two fixtures and location of the mapping pole in the target environment. The field compensation results were compared with a dipole PnO solution with and without polynomial-based PnO correction (i.e., a standard distortion compensation scheme). This experiment was conducted on each of the four datasets listed in Table III (mild, moderate, moderate-severe, and severe) to evaluate ICV performance over a range of application environments. A random sampling of 1000 field points, each with a random orientation, was created for the mapped volume and used to test the algorithms on the four datasets. This test assumes that all distortion in the field is caused by static object in or near the tracking volume.

The dipole solution was computed using the algorithm developed by Jones [21] based on (2) and (3). This approach is derived from the dipole model and is sensitive to distortions of the magnetic field, particularly the orientation measurement. The dipole solutions were used to generate a table that associated each PnO measurement with the true PnO. Two third-order polynomial functions were created from the tabulated data to generate correction factors for the measured PnO. The correction factors were then applied to the dipole PnO solution to find the polynomial-compensated solution. The field solution was determined by using an IVC generated secondary field map of the tracking volume to compensate the measured field before computation of the PnO solution. For this experiment, position solutions were bound to the tracking volume, forcing large errors to appear at the volume boundaries. This function is im-

plemented to provide usable data in all applications. Orientation solutions are bound to the normal Euler angle ranges.

The RMS and maximum PnO errors for each of the solution algorithms (see Table VIII) illustrate the performance of each approach at the four distortion levels tested. The dipole algorithm had small errors with mild distortion (4.96-mm RMS), which is a level that is tolerable by most applications. The errors increased as the distortion level increased but were well behaved until the severe category where hemisphere flips (rapid polarity changes in the position vector components) occurred. This instability in the position solution results in orientation solutions that are essentially unusable (642 mrad RMS). The polynomial-compensated solution improved performance for the mild and moderate cases but had larger errors for higher distortion levels than the dipole solution. Position error was nearly eliminated for the mild case (1.23 mm maximum) and reduced by more than 50% for the moderate case when compared with the dipole solution alone. Orientation errors were similarly reduced for these cases. However, the polynomial compensation is sensitive to the increasing error of the dipole solution, resulting in increased error for both position and orientation with moderate-severe distortion. The large orientation errors in the moderate-severe case (786 mrad maximum) make the solutions of questionable value. The essentially unbounded orientation errors for the severe case (3768 mrad maximum) results from the hemisphere flips in the dipole solution and offers no improvement over the uncompensated result. The polynomial compensation results are typical of position-based compensation methods which depend on the measured position as an input to the compensation algorithm. Good results can be obtained for mild and moderate distortion, but the increasing errors in the position measurement quickly result in unusable result. Other position-based methods (such as combining polynomial functions with an LUT) can extend the usability of this approach into the range of moderate distortion but are not effective with severe distortion.

The field solution uses the IVC system to construct a secondary field LUT for the tracked volume. In this case, the compensation is not reliant on the dipole position measurement, resulting in dramatically improved performance at all distortion levels. For mild distortion, PnO errors were reduced below the tracker specification (0.71 mm RMS), indicating that actual results will be similar to an undistorted environment. Results with moderate distortion were improved over the dipole and polynomial solutions, with very small PnO errors (0.22 mm RMS and 3.22 mrad RMS). The two low-distortion categories illustrate how well the field solution can work with an IVC LUT, providing improved performance over both the dipole and polynomial-compensated solutions. The benefit of the IVC approach is most apparent with high distortion (moderate-severe and severe cases). The field solution provided vastly improved results at these high distortion levels with a maximum position error of 3.84 mm and orientation error of 40.6 mrad under severe distortion. The low errors of the field solution across the entire spectrum of distortion levels indicate that the IVC system is accurately creating the secondary field LUT from the measured data.

TABLE VIII  
PnO ERROR VERSUS DISTORTION LEVEL

ALGORITHM	POSITION ERRORS (MM)				ORIENTATION ERRORS (M RADIANS)			
	MILD	MODERATE	MODERATE- SEVERE	SEVERE	MILD	MODERATE	MODERATE- SEVERE	SEVERE
DIPOLE SOLUTION	4.96 (11.20)	23.09 (51.18)	58.68 (125.76)	105.45 (195.31)	18.68 (47.31)	85.15 (220.79)	203.24 (524.94)	642.70 (3753.00)
POLYNOMIAL COMPENSATED	0.37 (1.23)	7.04 (18.49)	71.55 (171.05)	594.06 (1283.50)	3.35 (9.07)	20.6 (105)	317.23 (786.81)	1681.21 (3768.80)
FIELD SOLUTION	0.05 (0.17)	0.22 (0.72)	0.54 (1.93)	1.09 (3.84)	0.70 (2.59)	3.22 (12.08)	9.01 (32.88)	14.01 (40.61)

Note: Tabulated values are in RMS (MAX) format.

Our results do not provide performance comparable with the Polhemus mapper because of the several inaccuracies built into the system, including the interpolation fixture sensor placement, convergence problems with the cost function solver, and interpolation errors in the LUT generation process. The lack of a precise mounting surface on the sensors created a problem in locating the sensors on the interpolation fixture. We addressed this problem using an optimization process but were unable to correct all of the error. This problem could be eliminated using sensors that have been modified to present a precise mounting interface. There were some convergence problems with the position and orientation cost functions because of our choice of Levenberg–Marquardt minimization. The minimization has no information on the locality of the solution with which to reject unreasonable answers. Generally, this was not a problem in our work, since the position errors were small, but the outlier errors caused correspondingly large orientation errors. A Kalman-filter-based approach might be better suited to these tasks. Because of the manner of the data collection, the field data are located in concentric spheres spaced at 25.4-mm intervals. The interpolation result could be improved if a more varied dataset was created through more closely spaced sensors.

## V. CONCLUSION

In this study, we have presented a new method of calibration for ac magnetic trackers that can be built and operated without expensive equipment or highly trained individuals. The system was constructed for this study from readily available dimensional lumber and used to map a typical magnetic tracker application. The system was tested for four different distortion levels in the mapped volume, comparing PnO results of the dipole model, a polynomial-compensated solution, and a field-based solution. The dipole and polynomial-compensated solutions were found directly from measured field data, while the field solution used the IVC generated map. Test results indicate that the field-based solution is superior to the other methods in all the examined cases. Furthermore, the field solution was able to generate accurate PnO estimates in the severe distortion case when the other methods produced unusable results. The ability of the IVC system to support a successful field solution for all

distortion levels illustrates the applicability of this approach to calibrate an ac magnetic tracker.

## ACKNOWLEDGMENT

The authors would like to thank Polhemus, Inc., Colchester, VA, for support, time, and equipment used in this study. They would also like to thank H. Jones, J. Farr, and B. Himberg for their assistance.

## REFERENCES

- [1] K. Ali, C. Vanelli, J. Biesiadecki, M. Maimone, U. Y. Cheng, A. Martin, and J. Alexander, "Attitude and position estimation on the mars exploration rovers," in *Proc. IEEE Conf. Syst., Man, Cybern.*, Oct. 2005, vol. 1, pp. 20–27.
- [2] W. Birkfellner, F. Watzinger, F. Wanschitz, G. Enislidis, C. Kollmann, D. Rafolt, R. Nowotny, R. Ewers, and H. Bergmann, "Systematic distortions in magnetic position digitizers," *Med. Phys.*, vol. 25, no. 11, pp. 2242–2248, Nov. 1998.
- [3] W. Birkfellner, F. Watzinger, F. Wanschitz, R. Ewers, and H. Bergmann, "Calibration of tracking systems in a surgical environment," *IEEE Trans. Med. Imaging*, vol. 17, no. 5, pp. 737–742, Oct. 1998.
- [4] S. Bryson, "Measurement and calibration of static distortion of position data from 3D trackers," in *Proc. SPIE Conf. Stereoscopic Displays Appl. III*, Feb. 1992, pp. 244–255.
- [5] G. Burdea, "Invited review: The synergy between virtual reality and robotics," *IEEE Trans. Robot. Autom.*, vol. 15, no. 3, pp. 400–410, Jun. 1999.
- [6] J. C. K. Chou, "Quaternion kinematic and dynamic differential equations," *IEEE Trans. Robot. Autom.*, vol. 8, no. 1, pp. 53–64, Feb. 1992.
- [7] J. Day, D. Murdoch, and G. Dumas, "Calibration of position and angular data from a magnetic tracking device," *J. Biomech.*, vol. 33, no. 8, pp. 1039–1045, Aug. 2000.
- [8] M. Feuerstein, T. Reichl, J. Vogel, J. Traub, and N. Navab, "Magneto-optical tracking of flexible laparoscopic ultrasound: Model-based detection and correction of magnetic tracking errors," *IEEE Trans. Med. Imaging*, vol. 28, no. 6, pp. 951–967, Jun. 2009.
- [9] M. Fiala, "Pano-presence for teleoperation," in *Proc. IEEE/RSJ Int. Conf. Intell. Robots Syst.*, 2005, vol. 1, no. 4, pp. 2170–2174.
- [10] G. Fisher, "Electromagnetic tracker characterization and optimal tool design," M.S. thesis, John Hopkins Univ., Baltimore, MD, 2005.
- [11] R. Franke and G. Nielson, "Smooth interpolation of large sets of scattered data," *Int. J. Numerical Methods Eng.*, vol. 15, no. 11, pp. 1691–1704, 1980.
- [12] D. Frantz, A. Wiles, S. Leis, and S. Kirsch, "Accuracy assessment protocols for electromagnetic tracking systems," *Phys. Med. Biol.*, vol. 48, no. 14, pp. 2241–2251, Jul. 2003.
- [13] M. Ghazisaedy, D. Adamczyk, D. Sandin, R. Kenyon, and T. DeFanti, "Ultrasonic calibration of a magnetic tracker in a virtual reality space," in *Proc. IEEE Virtual Reality Annu. Int. Symp.*, Mar. 1995, pp. 179–188.

- [14] J. S. Goddard, Jr., "Pose and motion estimation from vision using dual quaternion-based extended Kalman filtering," Ph.D. dissertation, Dept. Electr. Eng., Univ. Tennessee, Knoxville, Dec. 1997.
- [15] F. S. Grant and G. F. West, *Interpretation Theory in Applied Geophysics*. New York: McGraw-Hill, 1965.
- [16] N. Hagemester, G. Parent, S. Husse, and J. Guise, "A simple and rapid method for electromagnetic field distortion correction when using two Fastrak sensors for biomechanical studies," *J. Biomech.*, vol. 41, no. 8, pp. 1813–1817, 2008.
- [17] H. Himberg and Y. Motai, "Head orientation prediction: Delta quaternions versus quaternions," *IEEE Trans. Syst., Man Cybern. B, Cybern.*, vol. 9, no. 6, pp. 1382–1392, Dec. 2009.
- [18] J. Hummel, M. Figl, C. Kollmann, H. Bergmann, and W. Birkfellner, "Evaluation of a miniature electromagnetic position tracker," *Med. Phys.*, vol. 29, no. 10, pp. 2205–2212, Oct. 2002.
- [19] J. Hummel, M. Bax, M. Figl, Y. Kang, C. Maurer, W. Birkfellner, H. Bergmann, and R. Shahidi, "Design and application of an assessment protocol for electromagnetic systems," *Med. Phys.*, vol. 32, no. 7, pp. 2371–2379, Jul. 2005.
- [20] M. Ikits, J. D. Brederson, C. D. Hansen, and J. M. Hollerbach, "An improved calibration framework for electromagnetic tracking devices," in *Proc. Virtual Reality Conf.*, Mar. 2001, pp. 63–70.
- [21] H. Jones, "Method and apparatus for determining remote object orientation and position," U.S. Patent 4 737 794, Apr. 1988.
- [22] J. Kofman, X. Wu, T. Luu, and S. Verma, "Teleoperation of a robot manipulator using vision-based human-robot interface," *IEEE Trans. Ind. Electron.*, vol. 52, no. 5, pp. 1206–1219, Oct. 2005.
- [23] V. Kindratenko, "A survey of electromagnetic position tracker calibration techniques," *Virtual Reality: Res., Dev. Appl.*, vol. 5, no. 3, pp. 169–182, 2000.
- [24] S. Livatino, G. Muscato, and F. Privitera, "Stereo viewing and virtual reality technologies in Mobile Robot Teleguide," *IEEE Trans. Robot.*, vol. 25, no. 6, pp. 1342–1355, Dec. 2009.
- [25] M. Livingston and A. State, "Magnetic tracker calibration for improved augmented reality registration," *Presence*, vol. 6, no. 5, pp. 532–546, Oct. 1997.
- [26] A. Milne, D. Chess, J. Johnson, and G. King, "Accuracy of an electromagnetic tracking device: A study of the optimal operating range and metal interference," *J. Biomech.*, vol. 29, no. 6, pp. 791–793, Jun. 1996.
- [27] K. Nakada, M. Nakamoto, Y. Sato, K. Konetishi, M. Hashizume, and S. Tamura, "A rapid method for magnetic tracker calibration using a magneto-optic tracker," *Med. Image Comput. Comput.-Assisted Intervention: Lect. Notes Comput. Sci.*, vol. 2879, pp. 285–293, 2004.
- [28] C. Nielson, M. Goodrich, and R. Ricks, "Ecological interfaces for improving mobile robot teleoperation," *IEEE Trans. Robot.*, vol. 23, no. 5, pp. 927–941, Oct. 2007.
- [29] M. Nixon, B. McCallum, W. Fright, and N. Price, "The effects of metals and interfering fields and on electromagnetic trackers," *Presence: Tele-Operators Virtual Env.*, vol. 7, no. 2, pp. 204–218, Apr. 1998.
- [30] F. Raab, E. Blood, T. Steiner, and H. Jones, "Magnetic position and orientation tracking system," *IEEE Trans. Aerosp. Electron. Syst.*, vol. AES-15, no. 5, pp. 709–718, Sep. 1979.
- [31] V. Kindratenko and W. Sherman, "Neural network-based calibration of electromagnetic tracking systems," *Virtual Reality*, vol. 9, no. 1, pp. 70–78, 2005.
- [32] R. Thompson, I. Reid, L. Munoz, and D. Murray, "Providing Synthetic views for teleoperation using visual pose tracking in multiple cameras," *IEEE Trans. Syst., Man, Cybern. A, Syst. Humans*, vol. 31, no. 1, pp. 43–54, Jan. 2001.
- [33] A. Wagner, K. Schicho, W. Birkfellner, M. Figl, R. Seemann, F. König, F. Kainberger, and R. Ewers, "Quantitative analysis of factors affecting intraoperative precision and stability of optoelectronic and electromagnetic tracking systems," *Med. Phys.*, vol. 29, no. 5, pp. 905–912, May 2002.
- [34] H. Wang and G. Jiang, "Study on sensor array applied in electromagnetic tracking system," in *Proc. IEEE/ICME Int. Conf. Complex Med. Eng.*, 2007, pp. 180–192.
- [35] X. Wu and R. Taylor, "A direction space interpolation technique for calibration of electromagnetic surgical navigation systems," in *Proc. Int. Conf. Med. Image Comput. Comput.-Assisted Intervention*, 2003, vol. 2879, pp. 215–222.



**Henry Himberg** received the B.S. degree in electrical and computer engineering from Clarkson University, Potsdam, NY, in 1982, the M.S. degree from the University of Vermont, Burlington, in 2005, and the Ph.D. degree in electrical and computer engineering from Virginia Commonwealth University, Richmond, in 2010.

He is currently a Principal Engineer with Polhemus, Inc., Colchester, VT. His research interests include signal processing, position/orientation measurement, and motion prediction.



**Yuichi Motai** (M'01) received the B.Eng. degree in instrumentation engineering from Keio University, Tokyo, Japan, in 1991, the M.Eng. degree in applied systems science from Kyoto University, Kyoto, Japan, in 1993, and the Ph.D. degree in electrical and computer engineering from Purdue University, West Lafayette, IN, in 2002.

He is currently an Assistant Professor with the Department of Electrical and Computer Engineering, Virginia Commonwealth University, Richmond, where he is also the Director of Sensory Intelligent Laboratory. His research interests include the broad area of sensory intelligence, particularly in medical imaging, pattern recognition, computer vision, and robotics.



**Arthur Bradley** received B.S., M.S., and Ph.D. degrees in electrical engineering from Auburn University, Auburn, AL, in 1990, 1992, and 1999, respectively.

He is currently a Senior Analog Engineer with Langley Research Center's Electronics Systems Branch at the National Aeronautics and Space Administration, Hampton, VA, where he is also the Director of Langley's Robotics and Intelligent Machines Laboratory. His research interests include robotic systems, cable noise-reduction techniques, and solid-state sensors. Current activities include the development of a novel amorphous fluid-filled robot and the integration of multispectral optical instruments onto an outdoor omnidirectional rover.